Accepted Manuscript
Version of record at: https://doi.org/10.1021/acsami.2c13852

Matrix Adhesiveness Regulates Myofibroblast Differentiation from Vocal Fold Fibroblasts in a Bio-orthogonally Cross-linked Hydrogel

Jiyeon Song, Hanyuan Gao, He Zhang, Olivia J. George, Ashlyn S. Hillman, Joseph M. Fox, and Xinqiao Jia*

Abstract

Repeated mechanical and chemical insults cause an irreversible alteration of extracellular matrix (ECM) composition and properties, giving rise to vocal fold scarring that is refractory to treatment. Although it is well known that fibroblast activation to myofibroblast is the key to the development of the pathology, the lack of a physiologically relevant in vitro model of vocal folds impedes mechanistic investigations on how ECM cues promote myofibroblast differentiation. Herein, we describe a bio-orthogonally cross-linked hydrogel platform that recapitulates the alteration of matrix adhesiveness due to enhanced fibronectin deposition when vocal fold wound healing is initiated. The synthetic ECM (sECM) was established via the cycloaddition reaction of tetrazine (Tz) with slow (norbornene, Nb)- and fast (trans-cyclooctene, TCO)-reacting dienophiles. The relatively slow Tz–Nb ligation allowed the establishment of the covalent hydrogel network for 3D cell encapsulation, while the rapid and efficient Tz–TCO reaction enabled precise conjugation of the cell-adhesive RGDSP peptide in the hydrogel network. To mimic the dynamic changes of ECM composition during wound healing, RGDSP was conjugated to cell-laden hydrogel constructs via a diffusion-controlled bioorthognal ligation method 3 days post encapsulation. At a low RGDSP concentration (0.2 mM), fibroblasts residing in the hydrogel remained quiescent when maintained in transforming growth factor beta 1 (TGF-β1)-conditioned media. However, at a high concentration (2 mM), RGDSP potentiated TGF-β1-induced myofibroblast differentiation, as evidenced by the formation of an actin cytoskeleton network, including F-actin and alpha-smooth muscle actin. The RGDSP-driven fibroblast activation to myofibroblast was accompanied with an increase in the expression of wound healing-related genes, the secretion of profibrotic cytokines, and matrix contraction required for tissue remodeling. This work represents the first step toward the establishment of a 3D hydrogel-based cellular model for studying myofibroblast differentiation in a defined niche associated with vocal fold scarring.

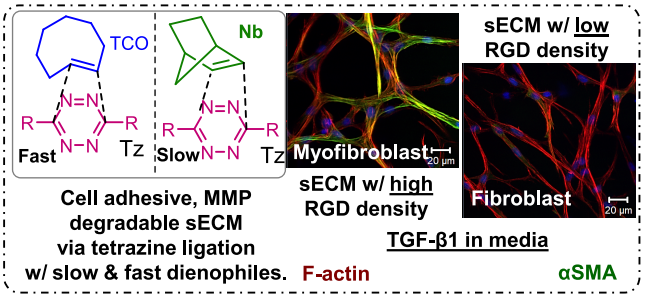

Keywords

Vocal fold fibroblasts, myofibroblasts, cell-adhesive peptide, transforming growth factor beta1, tetrazine ligation

1. INTRODUCTION

The vocal fold lamina propria is a loose connective tissue sandwiched between the overlying epithelium and the underlying vocalis muscle.[1] In adult humans, the lamina propria is further divided into the superficial, intermediate, and deep layers, according to the proportions and organizations of extracellular matrix (ECM) components. The complex layered structure determines the biomechanical properties of the vocal folds. The most pliable superficial layer consists of a largely amorphous matrix that contributes to the free flow of loose mucosa over the vocal fold during phonation. The intermediate and deep layers are mainly composed of a densely organized, intertwined fibrous network that permits energy transmission between the muscle and the epithelium. The vocal fold can be damaged by excessive mechanical stress, surgical interventions, and exposure to smoke, alcohol, or stomach acid, giving rise to vocal fold scarring with altered ECM compositions and viscoelasticity. The fibrous tissue disrupts the vibratory pattern and compromises the phonatory function.[2]

Fibroblasts found in all layers of the lamina propria are the main cellular component regulating scarring and healing processes.[3,4] Following tissue injury, fibroblasts differentiate into myofibroblasts for rapid repair of the ECM and reconstruction of the cellular microenvironment. Permanent fibronectin deposition in the superficial layer of the lamina propria is one of the representative responses to repeated vocal fold injuries.[5,6] The adhesive protein recruits fibroblasts to the wound site, promotes cell-ECM interactions, and facilitates the

Accepted Manuscript
Version of record at: https://doi.org/10.1021/acsami.2c13852

deposition of additional fibronectin matrix and other structural proteins such as collagen. While collagen gradually replaces the provisional fibronectin matrix during normal remodeling, fibronectin remains in the scarred tissue because of permanent tissue damage. The dysregulation of matrix turnover leads to an imbalance between pro-inflammatory and anti-inflammatory cytokines, further promoting myofibroblast differentiation.[7−10] The fibrotic ECM creates a pro-fibrotic niche that sustains fibrogenesis even when the chemical or mechanical insults are removed. Vocal fold scarring remains a significant therapeutic challenge as current clinical interventions do not result in long-term benefit. The development of efficacious therapies has been slow owing to the inaccessibility of the tissue, its susceptibility to surgical damage, and the scarcity of healthy human tissues. Thus, the establishment of an engineered vocal fold model that recapitulates the aberrant fibronectin deposition and fibroblast activation will not only improve our understanding of vocal fold scarring but also facilitate the development of new treatment options.

Synthetic extracellular matrices (sECMs) presenting pathophysiologically relevant biomechanical and biochemical cues to the resident cells are needed for a comprehensive understanding of how ECM signals influence myofibroblast differentiation.[11−13] Fibrous hydrogel networks derived from hyaluronic acid (HA) or dextran were utilized to investigate the effects of fiber mechanics and matrix degradation on myofibroblast mechanobiology.[14,15] Using collagen-based fibrous matrices, researchers examined how fiber diameter and pore size modulate myofibroblast differentiation.[16] Using hydrogels with covalently tethered anti- and pro-fibrotic growth factors, Ma et al. showed how the immobilized growth factors, singly or in combination, mediate fibroblast activation.[17] These studies shed light on how cell−ECM interactions contribute to fibroblast activation in the context of scarring and fibrosis of the liver,[14] lung,[15] breast,[16] and heart.[17]

We are interested in the development of a bioorthogonal hydrogel platform that captures the alteration of ECM compositions in scarred vocal folds. We previously demonstrated that synthetic matrices with temporally tunable properties (stiffness and adhesiveness) can be used to modulate stem cell morphology and functions.[18] The combination of a relatively slow thiol-acrylate Michael-type reaction with a rapid cycloaddition reaction between *s*-tetrazine (Tz) and *trans*-cyclooctenes (TCO) enabled the establishment of an initial cell-laden hydrogel construct and a time-delayed modification of the extracellular environment during cell culture. However, the synthesis of the polymer precursor bearing both acrylate and tetrazine functional groups is cumbersome and low-yielding. Additionally, the insufficient tetrazine incorporation in the polymer precursor limits the range of material properties that can be dynamically tuned. Notably, in addition to biocompatibility, bioorthogonality, high selectivity, and high efficiency, tetrazine reacts with various strained alkenes with tunable rates spanning several orders of magnitude.[19] Various dienophiles, including norbornene (Nb), bicyclononyne, and TCO, have been utilized for live-cell imaging,[20] protein labeling,[21] radiolabeling,[22] and biomaterials synthesis and fabrication.[23,24]

Herein, we describe a second-generation hydrogel platform encompassing quantitative and dynamic changes of matrix adhesiveness via tetrazine ligation with slow (Nb, $k_2 \approx 10^{-2}$-10^{0} M^{-1} s^{-1})[25] and fast (TCO, $k_2 \approx 10^{5}$ M^{-1} s^{-1})[19,26] dienophiles without the need for a second, independent cross-linking chemistry. The slow, off-stoichiometric Tz−Nb reaction was employed to create a primary network to encapsulate primary vocal fold fibroblasts, while the rapid Tz−TCO reaction was used to conjugate bioactive signals efficiently through the remaining tetrazine groups in the network. Temporal alteration of matrix composition was achieved via a diffusion-controlled bio-orthogonal ligation mechanism. Using this modular platform, we analyzed how alteration in matrix adhesiveness induces myofibroblast differentiation in the presence of transforming growth factor beta 1 (TGF-β1) at both transcript and protein levels. Additionally, the effect of a temporal increase of matrix adhesiveness on fibroblast activation was evaluated by immunofluorescence. Overall, we successfully applied tetrazine ligation to model the early stage of tissue fibrosis.

2. EXPERIMENTAL METHODS

2.1. Materials. Hyaluronic acid (sodium salt, 430 kDa) was a generous gift from Sanofi Genzyme Corporation. Small molecule TCO derivatives were prepared according to our previously reported procedures.[27,28] All amino acids were purchased from Aapptec. Oxyma and *N*,*N*′-diisopropylcarbodiimide (DIC) were purchased from CEM and Chem Impex, respectively. Dialysis membranes (MWCO: 10 kDa) were purchased from Spectrum Labs. Synthesis of Tz and TCO derivatives is detailed in the Supplementary Information.

2.2. Synthesis of Hydrogel Precursors. *s*-Tetrazine-modified hyaluronic acid (HA-Tz) and Nb/TCO-tagged bioactive peptides were synthesized following our previously reported methods.[29] Briefly, HA was reacted with 2-(4-(6-methyl-1,2,4,5-tetrazin-3-yl)-phenyl)acetohydrazide (MPTz-hydrazide; Figures S1−S3) through an *N*-(3-(dimethylamino)propyl)-*N*′-ethylcarbodiimide hydrochloride (EDC)-catalyzed coupling reaction at pH 4.75 to yield HA-Tz (Figure S4) with 22 mol % tetrazine incorporation, as quantified by UV−vis spectrophotometry and ^{1}H NMR spectroscopy (Figures S5 and S6). Separately, TCO nitrophenyl carbonate (Figures S7−S11) was conjugated to integrin-binding (GKGYGRGDSPG, RGD) or non-adhesive control (GKGYGRGESPG, RGE) peptides[30] through lysine amine to produce RGD-TCO and RGE-TCO (Figures S12−S24). Following our established peptide synthesis protocol,[29] a matrix metalloproteinase (MMP)-degradable peptide, with a sequence of Ac-KGGVPMS↓MRGGGGK-NH_2 (SMR), was prepared using a CEM Liberty Blue Peptide Synthesizer, cleaved using standard TFA/TIPS/H_2O (95,2.5,2.5) cocktail, and purified by reverse-phase high-performance liquid chromatography (RP-HPLC, Waters). The peptide was then allowed to react with norbornene-NHS ester (Figure S25−27) in the presence of triethylamine in dimethylformamide (DMF) at room temperature overnight (Figure S28). The crude peptide product (SMR-bisNb) was precipitated in ice-cold diethyl ether and further purified with HPLC using a gradient of acrylonitrile (ACN) in neutral water system. Peptide purity was analyzed at 214 nm using a Shimadzu Prominence Series HPLC. A Waters UPLC LC−MS/MS system with an ESI source (Xevo G2-S QTof) was used to confirm the molecular weight of the peptides. The composition and purity of the small-molecule intermediates and hydrogel precursors were confirmed by ^{1}H/^{13}C NMR, UV−vis, HPLC, and MS (Figures S29−S34).

2.3. Formation and Characterization of HA Hydrogels. *2.3.1. Hydrogel Preparation.* Stock solutions of HA-Tz (18 mg/mL), RGD-TCO (15 mg/mL), RGE-TCO (15 mg/mL), and SMR-bisNb (30 mg/mL) were separately prepared using 10 mM HEPES buffer containing 150 mM NaCl. The TCO solutions were mixed at a desired volume ratio and then added to the HA-Tz solution to tether cell-adhesive or non-adhesive motifs to the HA chains. The resultant solution was combined with the SMR-bisNb solution at a Tz/Nb molar ratio of 5:2 to initiate gelation at 37 °C. The final concentration of HA-Tz in the gel was 9 mg/mL. The final RGD concentration in the hydrogel (0.2 or 2 mM) was tuned by varying the ratio of RGD-TCO and RGE-TCO in feed while keeping the total peptide

concentration constant (RGD + RGE, 2 mM). Fifty minutes later, the hydrogel was submerged in HEPES buffer and maintained at 37 °C overnight to obtain a fully swollen construct. The equilibrium swelling ratio and peptide incorporation in the network were measured following our established procedure.[31] Separately, hydrogels containing excess tetrazine groups with an RGD concentration of 0.2 mM were prepared as described above. After the gelation was complete, RGD-TCO or RGE-TCO solution (0.5 mM) was added on top of the cross-linked hydrogels to initiate diffusion-controlled bioorthogonal ligation. Gels were maintained in the TCO bath at 37 °C for 24 h until the tetrazine chromophore completely disappeared.

2.3.2. Mechanical Properties. Hydrogel viscoelasticity was analyzed using a Discovery Hybrid Rheometer (DHR3; TA Instruments) equipped with an 8 mm parallel plate geometry. A premade hydrogel disk (140 μL, 8 mm in diameter) was placed on the geometry and loaded with 0.02 N normal force at 25 °C. A frequency sweep was conducted from 0.05 to 10 Hz at a 5% strain. The reported storage and loss moduli are the averaged values within the linear regime from 0.05 to 0.1 Hz.

2.4. Development and Characterization of Cell-Laden Hydrogel Constructs. *2.4.1. Cell Isolation and Maintenance.* Primary porcine vocal fold fibroblasts (VFFs) were isolated from freshly harvested porcine larynxes and cultured following the reported procedures.[32] VFFs were maintained in SCGM stromal cell growth medium (CC-3205; LONZA) supplemented with 1 ng/mL basic fibroblast growth factor (bFGF), 5 ng/mL insulin, and 1% (v/v) gentamicin sulfate−amphotericin. Passaging was conducted at 80% confluence using 0.05% (w/v) trypsin−EDTA. Trypsin was neutralized using a trypsin soybean inhibitor (T6522; Sigma-Aldrich). All experiments were conducted within passages 1−4.

2.4.2. Cell Encapsulation and 3D Culture. Dilute HA-Tz solution was sterile-filtered (with 0.2 μm filters) prior to lyophilization and maintained under aseptic conditions thereafter. Reconstituted peptide/HEPES solutions were sterilized using 0.2 μm syringe filters. All hydrogel precursors were mixed homogeneously before being combined with the cell suspension. VFFs were encapsulated at 2 × 10^6 cells/mL, and the mixture was transferred to 48-well glass-bottom MatTek plates (35 μL) or 10.5 mm cell culture inserts (200 μL). The 3D cultures were maintained in media without bFGF. Twenty-four hours later, media was supplemented with 5 ng/mL of TGF-β1, and the cultures were extended up to 14 days with media refreshment every other day. Constructs cultivated in TGF-β1-free media were included as controls.

2.4.3. Cell Viability. Cell viability was analyzed by live/dead staining using calcein-AM (1:1000 dilution), ethidium homodimer (1:2000 dilution), and Hoechst 33342 (1:500 dilution) on days 3, 7, and 14. Confocal images were captured as 99.44 μm z-stacks with 2.925 μm slices using a Zeiss LSM 880 with a 10× objective lens. Cell viability was quantified using ImageJ by counting the total number of cells (stained by Hoechst) and dead (stained by ethidium homodimer) cells in each image of maximum intensity projection produced by Zeiss's Zen software. A total of three biological repeats were performed at each time point.[31]

2.4.4. Metabolic Activity. Cell metabolism was assessed using the PrestoBlue Cell Viability Reagent (A13262, Thermo Fisher Scientific) on days 3, 7, and 14. PrestoBlue was diluted in cell culture media at 10% (v/v). After aspirating media, each hydrogel construct was incubated with 220 μL of PrestoBlue solution at 37 °C for 4 h. Next, 90 μL of the solution from each sample was transferred to a 96-well plate, and fluorescence was measured using a SpectraMax i3x Multi-Mode Microplate Reader at 585 nm. Data were normalized with respect to low RGD samples without TGF-β1 treatment on day 3.

2.4.5. Immunofluorescence. Cell-laden hydrogel constructs were fixed with 4% (w/v) paraformaldehyde in PBS for 50 min and then permeabilized with 0.2% (v/v) Triton X-100 for 15 min. Hydrogel samples were blocked with 3% (w/v) bovine serum albumin overnight at room temperature. Subsequently, FITC-labeled antibody for α-smooth muscle actin (F3777, Sigma-Aldrich) and Alexa Fluor 568-labeled phalloidin (A12380, Thermo Fisher Scientific), diluted at 1:200 and 1:400, respectively, were incubated with the samples overnight at room temperature. DAPI was used to stain the nuclei at 1:200 dilution with 30 min incubation. Confocal imaging was performed using a Zeiss LSM 880 equipped with an Airyscan detector in Fast Airyscan mode with a 25× objective lens. Images were captured from the middle portion of the gel as 70.87 μm z-stacks with a 0.492 μm z axis step size. αSMA expression was quantified with Fiji ImageJ software using integrated fluorescent signal density for αSMA and F-actin. The sum of the fluorescent intensity for αSMA was normalized to that for F-actin with the same threshold setting in each channel.[33] In addition, αSMA and F-actin colocalization was quantified by calculating the Mander's coefficient (M2) from maximum intensity projections using Fiji ImageJ. To distinguish the actin stress fibers from diffused cytoplasmic staining, a manually determined threshold was uniformly applied to αSMA and F-actin channels, respectively, using JACoP plugins. The sum of colocalized green (for αSMA) and red (F-actin) signal was divided by the sum of the red signals.

2.4.6. Gene Expression. After 3, 7, and 12 days of culture, VFF-laden HA hydrogel constructs were flash-frozen in a dry ice/isopropanol slurry and stored at −80 °C for further processing. The frozen hydrogels were completely homogenized in TRIzol, followed by the addition of chloroform before incubating samples for 3 min at room temperature. The RNA containing the colorless aqueous phase was collected after centrifugation at 4 °C for 20 min at 15,000 g. Further RNA purification was performed using an RNA Clean & Concentrator-5 Kit (R1013, Zymo Research) according to the manufacturer's protocol. The purified RNA was reverse-transcribed to cDNA using a QuantiTect Reverse Transcription Kit (Qiagen). Real-time quantitative polymerase chain reaction (qPCR) was performed using a combination of 4 ng of cDNA templates, 400 nM primers, and SYBR Green Master Mix (2×, 10 mL) in an ABI 7300 real-time PCR system. The primer sequences are available in Table S1. The porcine COL1A2, ITGA5, and CTGF primers were purchased from Bio-Rad Laboratories. Hypoxanthine-guanine phosphoribosyltransferase (*HPRT*) was used as a reference gene.[34] The fold change was processed by qbase+ software (Biogazelle). A total of three biological repeats were analyzed for each gel composition.

2.4.7. ELISA and Protein Antibody Array. Cell culture supernatant was collected in low protein-binding microcentrifuge tubes on day 14 and stored at −80 °C. The expression of 20 porcine cytokines was semi-quantitatively examined using Porcine Cytokine Array GS4 (GSP-CYT-4-1, RayBiotech) and Porcine Cytokine Antibody Array A (ab197479, Abcam) according to the manufacturer's protocol. Fluorescent signals were recorded using an iBright FL1500 Imaging System (Invitrogen). The highly secreted cytokines were further quantified using an enzyme-linked immunoassay (ELISA). The total amount of secreted IL-6 (porcine, DY686, R&D Systems), IL-8 (porcine, DY535, R&D Systems), VEGF-A (porcine, ELP-VEGFA-5, RayBiotech), procollagen 1α1 (human, DY6220−05, R&D Systems), and TIMP2 (human, DY971, R&D Systems) was determined using a SpectraMax i3x Multi-Mode Microplate Reader according to the manufacturer's protocol. The secretion levels were normalized to the total protein content determined by bicinchoninic acid (BCA) assay (Figure S38) using a Micro BCA Protein Assay Kit (23235, Thermo Fisher Scientific) on a SpectraMax i3x Multi-Mode Microplate Reader at 562 nm. The homology analysis between the human and the porcine sequences showed 92.3% for procollagen 1α1 and 97.3% for TIMP2, confirming the cross-reactivity of the antibodies.

2.4.8. Protein Extraction and Western Blotting. The frozen constructs, prepared with the same method designed for RNA extraction, were crushed with a polypropylene pestle and then treated with RIPA buffer (R0278, Sigma-Aldrich) containing 1% (v/v) of halt protease and phosphatase inhibitor cocktail (78442, Thermo Scientific). The mixture was incubated at 4 °C for 1 h, followed by centrifugation at 4 °C for 20 min at 13,000 g. The supernatant was collected, and the total protein was quantified as described above. The cell lysate was stored at −80 °C until Western blotting was performed. For Western blotting analysis, the cell lysate was mixed with 3× blue loading buffer (56036, Cell Signaling Technology) and 150 mM dithiothreitol (10708984001, Sigma-Aldrich) to make 1.5−15 μg of

Accepted Manuscript
Version of record at: https://doi.org/10.1021/acsami.2c13852

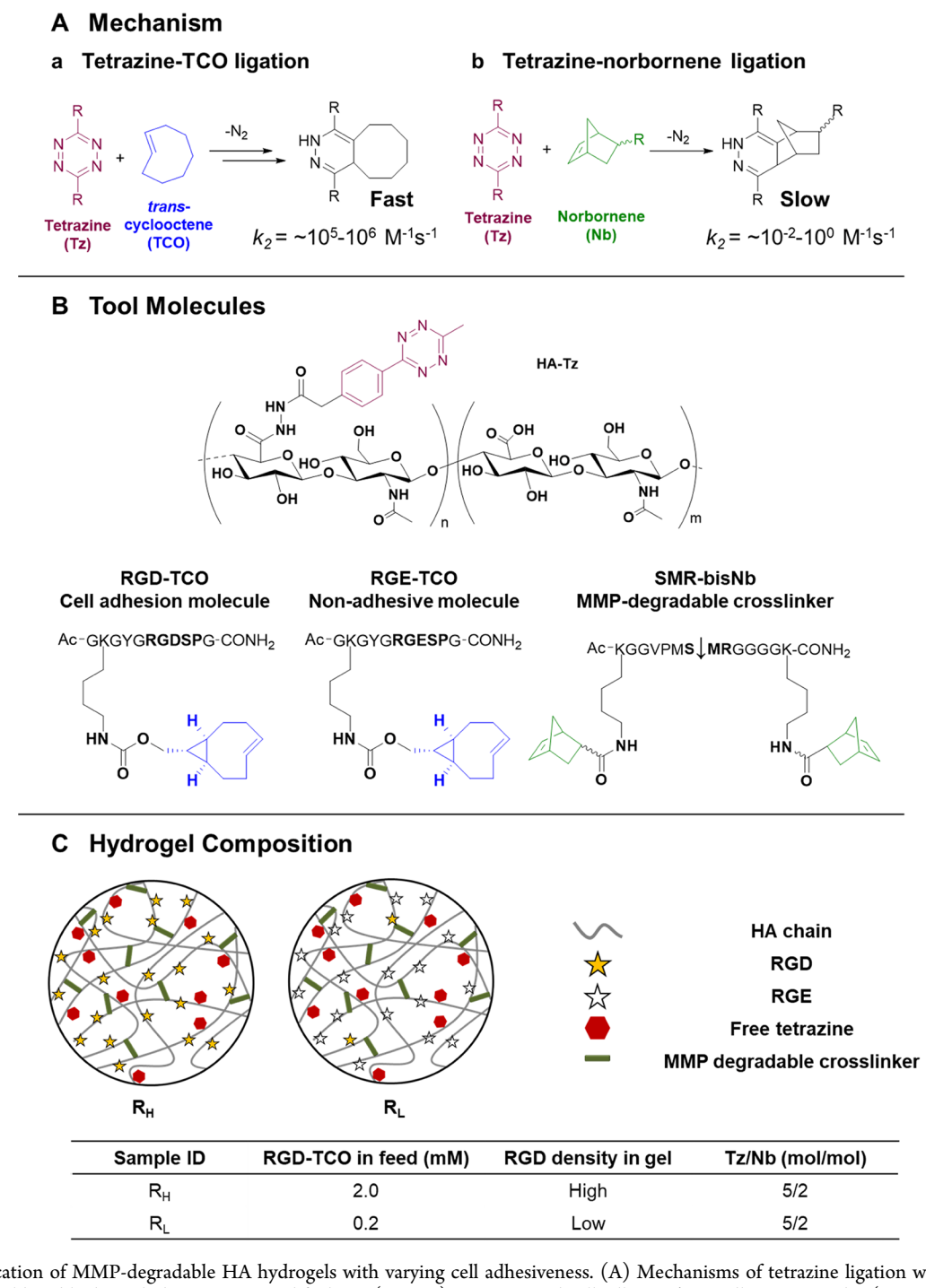

Sample ID	RGD-TCO in feed (mM)	RGD density in gel	Tz/Nb (mol/mol)
R_H	2.0	High	5/2
R_L	0.2	Low	5/2

Figure 1. Fabrication of MMP-degradable HA hydrogels with varying cell adhesiveness. (A) Mechanisms of tetrazine ligation with TCO and Nb. (B) Hydrogel building blocks include tetrazine-modified HA (HA-Tz), TCO-tagged cell adhesive/non-adhesive peptides (RGD/RGE-TCO), and Nb-functionalized MMP-degradable cross-linker (SMR-bisNb). (C) Hydrogels with the same stiffness but different adhesiveness were prepared.

loading samples. The loading samples were incubated for 5 min at room temperature, followed by 10 min incubation at 95 °C. The solution was centrifuged at 15,000 *g* for 30 s at room temperature before loading to 4−20% mini-protean TGX stain-free protein gels (4561093, Bio-Rad Laboratories). The SDS-PAGE gel in tris-glycine-SDS buffer (1610732, Bio-Rad Laboratories) was supplied with 50 V for 30 min at 4 °C, followed by 200 V for 40 min at 4 °C. The protein samples were further transferred to the PVDF transfer membrane (PI88518, Thermo Fisher Scientific) incubated with 1× tris-glycine transfer buffer (12539S, Cell Signaling Technology) at 4 °C for 2 h under 70 V. The membrane was stained with Revert 700 total protein stain (926-11010, LI-COR Biosciences) according to the manufacturer's protocol and imaged using an iBright FL1500 Imaging System (Invitrogen). Membranes were blocked with Superblock T20 (37536, Thermo Fisher Scientific) overnight at 4 °C. Primary antibody αSMA (ab7817, Abcam) was diluted in 5% (w/v) skim milk/TBST at 1:1000 and incubated with membrane samples overnight at 4 °C. Separately, MLC2 antibody (8505S, Cell Signaling Technology) was diluted in 5% (w/v) skim milk/TBST at 1:500 and incubated with samples for 2 days at 4 °C. For secondary staining, horseradish peroxidase (HRP)-linked antibody was used at 1:10,000 for the αSMA sample and 1:5000 for the MLC2 sample for 1 h at room temperature. Chemiluminescent signals were recorded using an iBright FL1500 Imaging System with VisULite MAX ECL Western Blotting Substrate (VL022−200, R&D Systems). Western blotting data were analyzed using ImageJ. Total protein was used as the

Accepted Manuscript
Version of record at: https://doi.org/10.1021/acsami.2c13852

internal control to normalize each protein lane since the expression level of housekeeping proteins can vary depending on samples and the experimental conditions.[35,36] The total proteins were stained using Revert 700 total protein stain (926-11010, LI-COR Biosciences) and imaged in the 700 nm channel, and the chemiluminescent signal for the target protein was normalized to that for all proteins found in the cell lysate.

2.4.9. Hydrogel Contraction. Hydrogel contraction was evaluated by photographing the cell-laden gel disks using a digital camera and measuring the sample diameter with ImageJ. The degree of hydrogel contraction was calculated by comparing the original gel dimension to that for the day 14 construct.

2.5. Statistical Analysis. Statistical analysis was performed using Student's *t* test, one-way ANOVA, or two-way ANOVA. The one-way or two-way ANOVA analysis was followed by Tukey' HSD post hoc for pairwise comparison. A *p*-value of less than 0.05 was considered to be significantly different. All quantitative analyses were conducted on data sets in which $n \geq 3$. For the characterization of cellular constructs, quantitative results were obtained from three biological repeats. Error bars represent standard error of the mean (SEM) from multiple repeats. Statistical interpretations were made using GraphPad Prism version 9.

3. RESULTS AND DISCUSSION

3.1. Bioorthogonal Tetrazine Ligation Enables Facile Preparation of sECM. Biomimetic hydrogels were produced using tetrazine-functionalized HA (HA-Tz), along with Nb- and TCO-tagged bioactive peptides (Figure 1). To enable cell-mediated matrix remodeling, metalloproteinase (MMP)-cleavable peptide with a sequence of VPMS↓MRGG (SMR, ↓ denotes the cleavage site) was employed to establish the covalent network. To promote integrin-mediated cell−matrix interaction, fibronectin-derived RGD peptide was conjugated to the network as elastically inactive dangling chains.[18,29] Hydrogels were prepared off-stoichiometrically, with a Tz to Nb molar ratio of 5/2, to generate constructs with stiffness comparable to that of vocal fold mucosa (the epithelium and the superficial layer of the lamina propria combined)[37,38] and to enable the creation of a predictable amount of residual tetrazine groups for RGD tagging via bulk reaction during gelation or at the gel−liquid interface after the primary network was established. To maintain the overall network structure and mechanical properties, non-adhesive RGE peptide was included in the reaction mixture such that the total concentration of the dangling peptides (RGD + RGE) was the same (2 mM) across different gel formulations (Figure 1C). Under these conditions, hydrogels with high (R_H) and low (R_L) RGD concentrations were readily prepared by varying RGD/RGE mixing ratio in feed. In our design, TCO, an avid dienophile that is conformationally strained,[19] was conjugated to RGD/RGE for rapid and efficient peptide conjugation. On the other hand, Nb, a much less reactive dienophile, was coupled to the MMP degradable peptide to produce the MMP-bisNb cross-linker for the preparation of a homogeneous network. Although tetrazine−TCO ligation is one of the highly reactive and efficient bio-orthogonal chemistries, this reaction is not suitable for hydrogel preparation via bulk gelation as the fast kinetics precludes effective mixing of hydrogel precursors and cell suspensions, resulting in an inhomogeneous hydrogel network architecture and subsequently inconsistent cellular responses.[39]

To quantify peptide conjugation efficiency, hydrogels were prepared with 2 mM RGD or RGE-TCO. HPLC analysis was performed on the aqueous bath equilibrated with the fully swollen hydrogel, thus containing unconjugated, freely diffusible peptide species, if any. Using standard curves constructed from measured integrated peak areas for the respective peptide species (Figure S35), the concentration of the unconjugated peptide in the bath was determined. After 24 h of equilibrium in HEPES, over 99% of the peptide was retained in the hydrogel constructs with both RGD-TCO and RGE-TCO (Figure 2A). Thus, the highly efficient tetrazine/

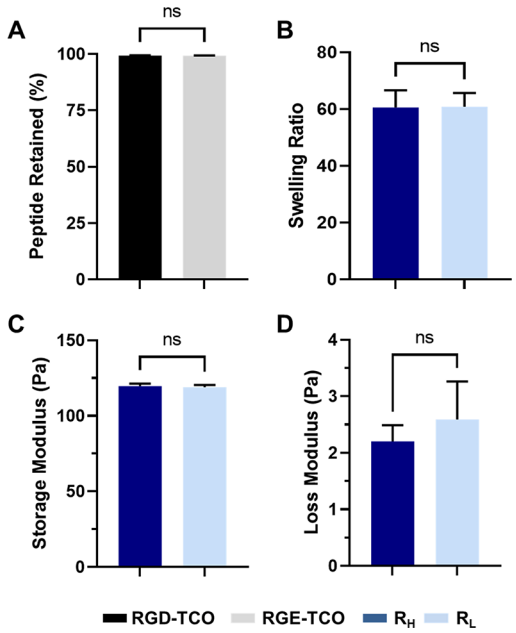

Figure 2. Characterization of hydrogel composition (A), swelling (B), and mechanical properties (C, D). (A) Peptide retention in hydrogels prepared using TCO-tagged RGD or RGE. Hydrogels were equilibrated in HEPES for 24 h before the solution was aspirated for HPLC analysis. Each hydrogel was conjugated with 2 mM of peptide. (B) Equilibrium swelling ratio for gels R_H and R_L. (C, D) Rheological analyses of gels R_H and R_L. Gels R_H and R_L exhibit similar storage and loss moduli. $n = 3$; ns: nonsignificant, $p > 0.05$, determined by Student's *t* test. Error bars represent the standard error of the mean.

TCO reaction allowed quantitative incorporation the integrin-binding ligand in the synthetic matrix without the need for post-gelation wash to remove any free, unreacted species that can competitively block integrin binding during 3D culture.

The hydrogels swelled rapidly in HEPES buffer, reaching an equilibrium swelling ratio of 60.6 ± 6.1 and 60.8 ± 4.9 for the R_H and R_L, respectively (Figure 2B). Examination of hydrogel viscoelasticity by oscillatory rheommetry revealed that these gels also exhibited similar mechanical properties (Figure 2C, D), with R_H and R_L having average storage (G')/loss (G'') moduli of 119.7 ± 1.6 Pa/2.2 ± 0.3 Pa and 119.0 ± 1.4 Pa/2.6 ± 0.7 Pa, respectively. These values are comparable with that measured for human vocal fold mucosa (10−100 Pa).[38] Representative frequency sweep results are shown in Figure S36. Taken together, the bio-orthogonal approach enabled the development of sECM with consistent mechanical properties but variable RGD densities.

3.2. sECM Supports the Growth of Vocal Fold Fibroblasts in 3D. Primary VFFs were expanded on conventional tissue culture polystyrene (TCPS) in SCGM containing bFGF to promote fibroblast proliferation as well as to prevent stiff substrate-induced myofibroblast differentiation during 2D culture.[40,41] To establish 3D cell-laden gel

Accepted Manuscript
Version of record at: https://doi.org/10.1021/acsami.2c13852

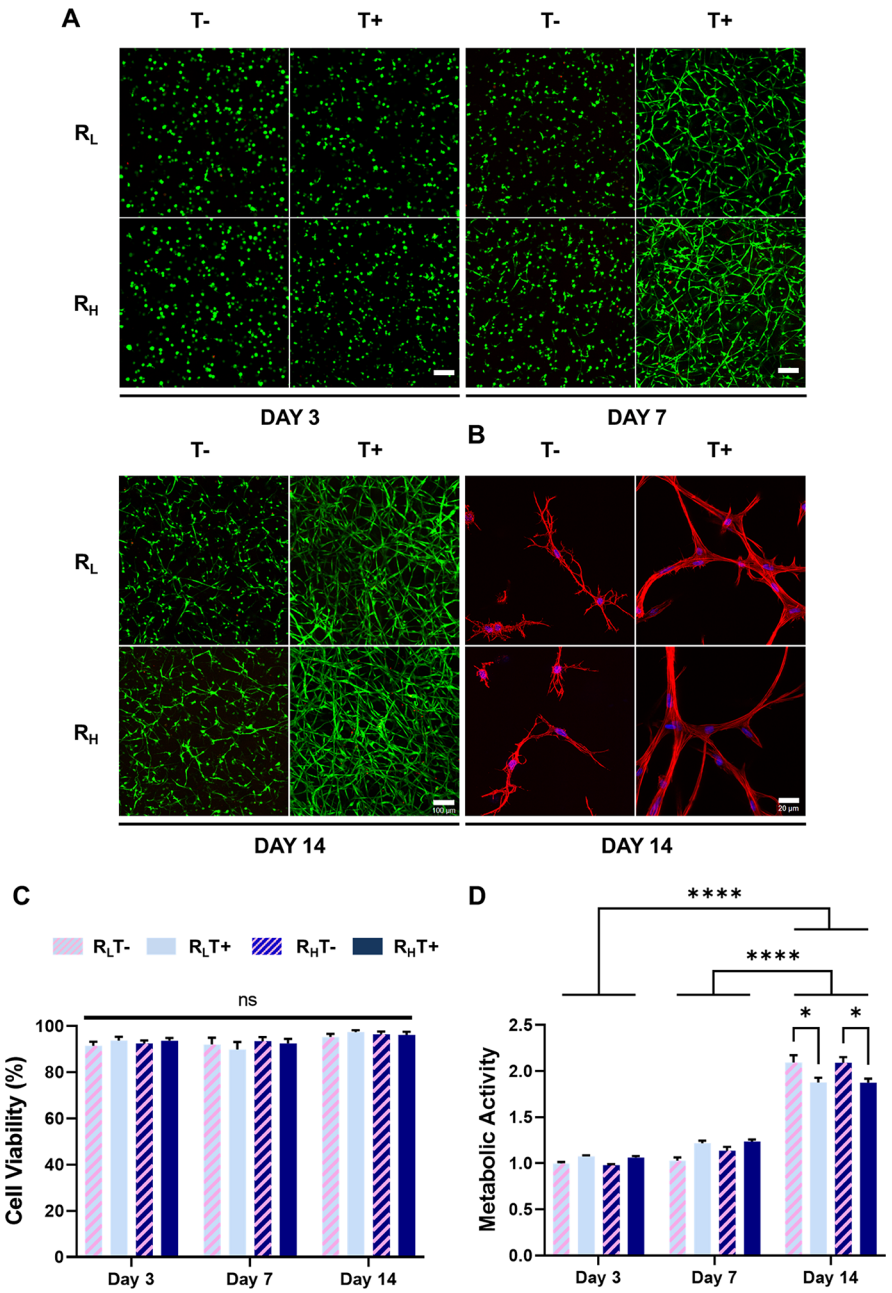

Figure 3. Characterization of 3D cultures in terms of viability (A, C), morphology (B), and metabolic activities (D). (A) Confocal images of VFFs stained by calcein AM (green) and ethidium homodimer-1 (EthD, red) after 3, 7, and 14 days of culture. Scale bar, 100 μm. (B) Confocal images of VFFs stained by F-actin (red) and DAPI (blue) after 14 days of culture. Scale bar, 20 μm. (C) Quantitative cell viability analysis based on calcein/EthD-stained constructs using ImageJ. ns: nonsignificant, determined by two-way ANOVA. (D) Quantification of cell metabolism by PrestoBlue assay, as fold change relative to the R_LT- level on day 3. *$p < 0.05$, ****$p < 0.0001$, determined by two-way ANOVA. All error bars represent the standard error of the mean.

constructs, VFFs were encapsulated in homogeneously HA gels with high (R_H) and low (R_L) RGD concentrations. The encapsulated VFFs were subjected to 24 h of bFGF starvation to remove the antagonist effect of bFGF toward myofibroblast differentiation.[41] Thereafter, VFFs were cultivated for 14 days in the presence (T+) or absence (T-) of TGF-β1, a profibrotic cytokine known to stimulate myofibroblast differentiation.[42] Live/dead staining (Figure 3A) shows that cells maintained in the synthetic ECM gradually transformed from a round shape at day 3 to a spindle-shaped morphology at day 14 both at low and high RGD concentrations. In agreement with prior findings, cell attachment and spreading in our synthetic matrices were facilitated by RGD−integrin engagement and cell-mediated matrix remodeling by secreted MMPs.[18,23,43] With TGF-β1 treatment (R_HT+ and R_LT+), cells formed a dense, interconnected cellular network by day 14, whereas those without TGF-β1 treatment (R_HT- and R_LT-) remain individually dispersed. F-actin staining (Figure 3B) shows that in the absence of TGF-β1, VFFs developed filopodia-like processes with parallel bundles of actin filaments traversing the entire cell body by day 14, both at high and low RGD concentrations (i.e., R_LT- and R_HT-). With TGF-β1 treatment, the F-actin filamentous structures became longer and more extended.[44] Quantitative image analysis of the live/dead results

Accepted Manuscript
Version of record at: https://doi.org/10.1021/acsami.2c13852

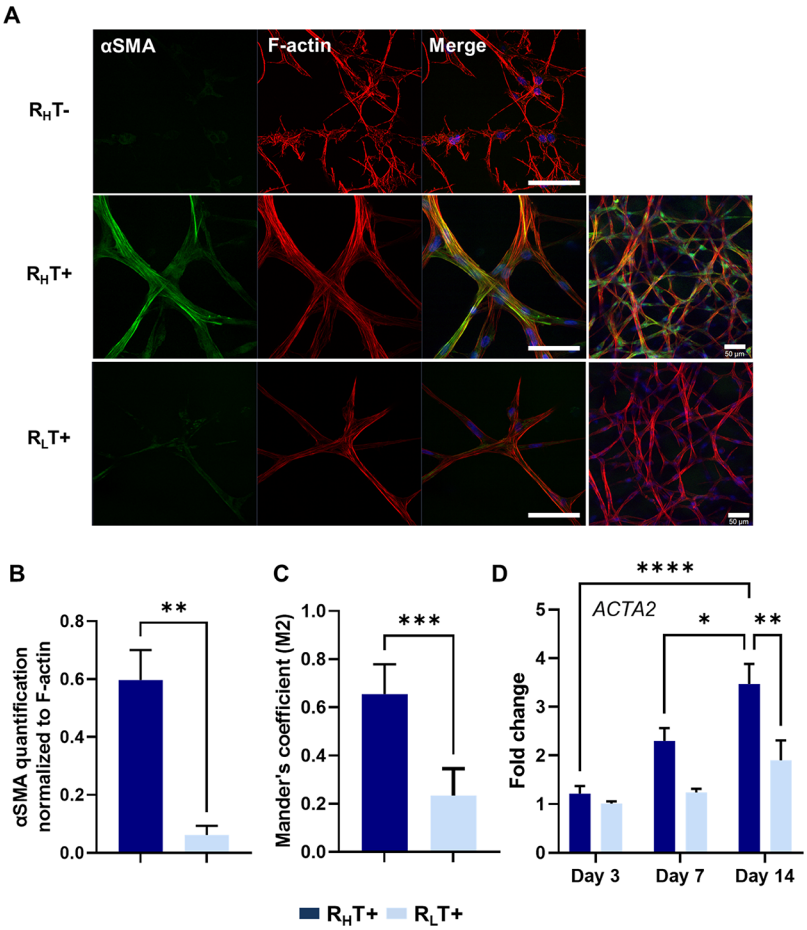

Figure 4. Characterization of αSMA expression in 3D cultures by immunocytochemistry (A) and image analysis (B,C), and qPCR (D). (A) Representative confocal images of day 14 constructs showing αSMA, F-actin, and nuclei stained green, red, and blue, respectively. Scale bar, 50 μm. (B) Quantification of αSMA expression as the integrated density ratio between αSMA and F-actin signals in R_HT+ and R_LT+ cultures. The sum of the fluorescent intensities of αSMA was normalized to that for F-actin. $^{**}p < 0.01$, determined by Student's t test. $n = 5$. (C) Quantification of Mander's coefficient (M2) in R_HT+ and R_LT+ cultures. M2 is defined as the fraction of αSMA overlapped with F-actin bundles, with 0 indicating no colocalization and 1 corresponding to complete colocalization. $^{***}p < 0.001$, determined by Student's t test. $n = 5$. (D) Temporal *ACTA2* expression in R_HT+ and R_LT+ cultures by qPCR. Expression was normalized to the R_LT+ level on day 3. $^{*}p < 0.05$, $^{**}p < 0.01$, and $^{****}p < 0.0001$, determined by two-way ANOVA. $n = 9$ (three biological repeats, each with three technical repeats). All error bars represent standard error of the mean.

revealed high percentages of viable cells (>89%) under all four conditions throughout the 14 days of culture (Figure 3C), confirming the cytocompatiblity of the bioorthogonal hydrogel platform.

PrestoBlue assay was conducted to assess the effects of inductive signals, both soluble (TGF-β1) and immobilized (RGD), on cell metabolism and indirectly, cell proliferation, in the engineered matrices (Figure 3D). No significant cell proliferation was observed on days 3−7. In the absence of TGF-β1, cell metabolism increased by 2.09 ± 0.08 and 2.09 ± 0.06 folds from day 3 to day 14 for low (R_LT-) and high RGD (R_HT-) concentrations, respectively. However, in the presence of TGF-β1, cell metabolism increased by 1.88 ± 0.05 and 1.87 ± 0.04 folds from day 3 to day 14 for low (R_LT+) and high RGD (R_HT+) concentrations, respectively. Cross comparison between T- and T+ conditions show that TGF-β1 significantly ($p < 0.05$) suppressed cell proliferation on day 14 for both R_H and R_L conditions. Chen et al. cultured human VFFs in HA/gelatin gels cross-linked by poly(ethylene glycol) and found that TGF-β1 at 5 ng/mL did not significantly increase cell proliferation, although significant cell proliferation was observed on 2D TCPS and HA/gelatin cultures at 0.1 to 20 ng/mL.[45] TGF-β1 is multifunctional, capable of regulating cell proliferation, differentiation, motility, and organization. Depending on cell types and culture conditions, TGF-β1 can be mitogenic or antimitogenic.[46,47] In our case, TGF-β1 stimulated the development of extended cytoskeleton structures rather than increasing cell proliferation. The development of the interconnected cellular network may be indicative of myofibroblast differentiation (see Section 3.3).[44]

3.3. sECM with R_H Primes VFFs for TGF-β1-Induced Myofibroblast Differentiation. To investigate whether the reduced proliferation accompanied the differentiation of VFFs, the expression of α-smooth muscle actin (αSMA), a myofibroblast marker, was measured by immunofluorescence and qPCR. In the absence of TGF-β1, isolated cells in gels with high adhesiveness (R_HT-) displayed diffuse and very weak αSMA staining at day 14 (Figure 4A). By contrast, αSMA-positive (αSMA+) cells were abundant in R_HT+ cultures, and the staining was concentrated and strong. As shown in Figure 4B, αSMA expression was significantly ($p < 0.01$) higher in

Accepted Manuscript
Version of record at: https://doi.org/10.1021/acsami.2c13852

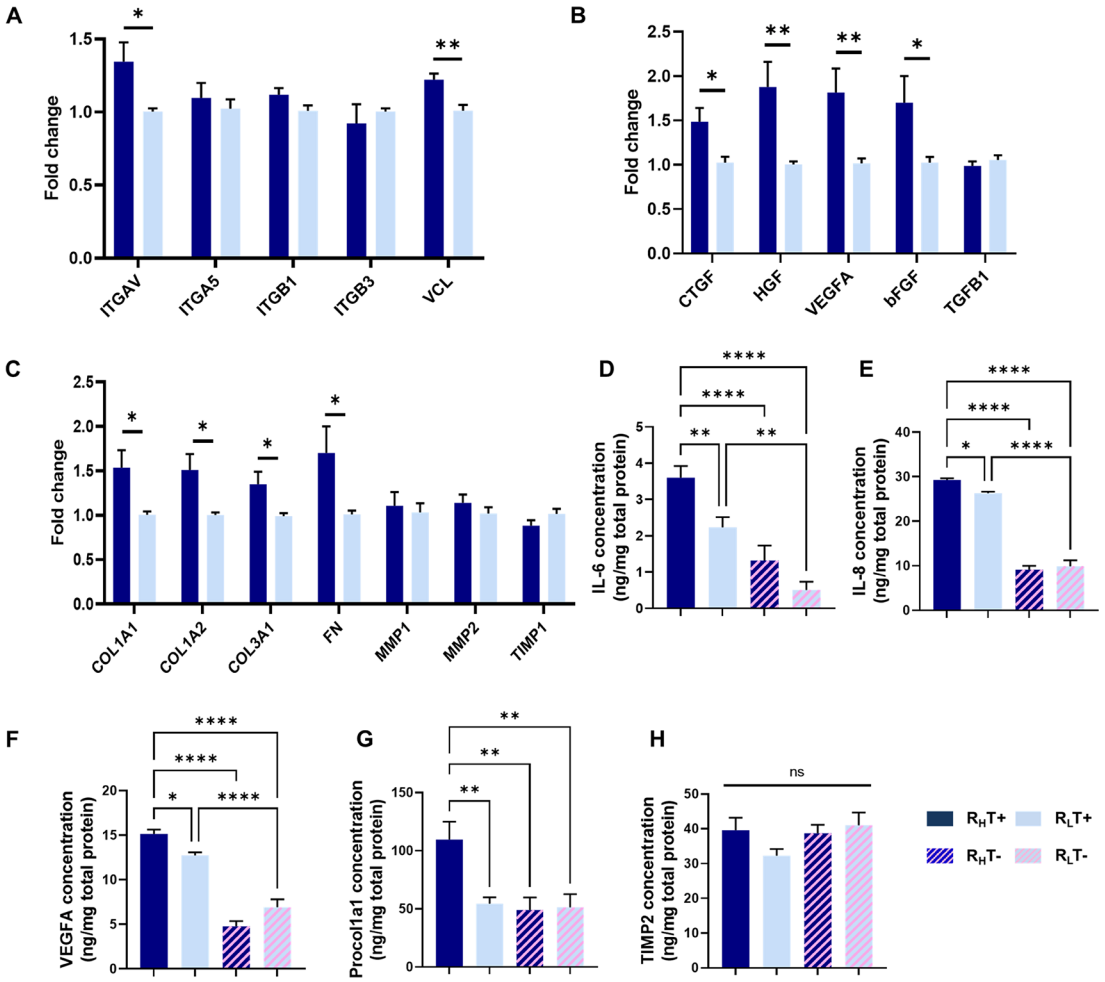

Figure 5. Effects of culture conditions on VFF gene expression and cytokine secretion. (A–C) qPCR analysis of day 14 constructs for the expression of proteins involved in cell-ECM adhesion (A), pro-fibrotic growth factors (B), and ECM proteins (C) as a function of RGD concentrations. Fold change normalized to the R_LT+ level on day 14. (D–H) Characterization of day 14 constructs for cellular secretion of IL-6 (D), IL-8 (E), VEGFA (F), pro-collagen 1α1 (G), and TIMP2 (H) by ELISA. *$p < 0.05$, **$p < 0.01$, and ****$p < 0.0001$, determined by Student's *t* test or one-way ANOVA where appropriate. ns: nonsignificant. All error bars represent the standard error of the mean.

R_HT+ (0.60 ± 0.10) cultures than the R_LT+ counterpart (0.06 ± 0.03).

The overlapping of αSMA (green) and F-actin (red) signals confirms the incorporation of αSMA in cytoskeletal filaments, required for generating contractile forces during tissue remodeling.[48] Interestingly, TGF-β1-induced myofibroblast differentiation was strongly dependent on matrix adhesiveness; cells maintained with TGF-β1-conditioned media in gels with a low RGD concentration (R_LT+) were weakly stained for αSMA even though an extended cellular network was formed. Thus, our results suggest that both high RGD density and the presence of soluble TGF-β1 are required for the development of αSMA+ stress fibers in 3D. To quantify the degree of αSMA incorporation in F-actin filaments, Mander's colocalization coefficient (M2) was measured using ImageJ as the fraction of αSMA staining overlapped with that for F-actin staining.[49,50] As shown in Figure 4C, R_HT+ cultures exhibited significantly higher ($p < 0.001$) M2 values (0.65 ± 0.06) than R_LT_+ cultures (0.23 ± 0.05).

Consistent with the image analysis, temporal gene expression profiling showed an upregulation of *ACTA2* expression for both R_HT+ and R_LT+ cultures during 14 days of culture, although their expression levels were significantly different (Figure 4D). By day 14, *ACTA2* expression in R_LT+ cultures increase moderately, with an average of 1.90 ± 0.41 folds relative to the day 3 level of R_LT+ cultures. On the other hand, *ACTA2* expression in R_HT+ cultures was significantly ($p < 0.0001$) upregulated (3.47 ± 0.41 folds) on day 14 relative to day 3 level of R_LT+ cultures. On day 14, *ACTA2* expression was significantly ($p < 0.01$) higher in R_HT+ than R_LT+. Collectively, R_HT+ cultures produced cells with the highest level of αSMA expression both at the mRNA and protein levels. In other words, sECM with a high RGD density primes fibroblasts for activation to myofibroblasts in the response to TGF-β1. Because VFFs interact with the matrix through integrin engagement with the immobilized RGD peptide, cells in R_HT_+ cultures can bind the matrix more avidly than those in R_LT+, thereby transmitting a higher level of intracellular forces to the extracellular milieu. Consequently, these cells are more contractile and more actively participate in matrix remodeling.[48,51,52]

We further evaluated the effects of RGD density on the expression of genes encoding integrins, focal adhesion complexes, growth factors, and ECM proteins by qPCR (Figure 5). It has been reported that TGF-β1 modulates the integrin-mediated cell adhesion and signaling pathways by

Accepted Manuscript
Version of record at: https://doi.org/10.1021/acsami.2c13852

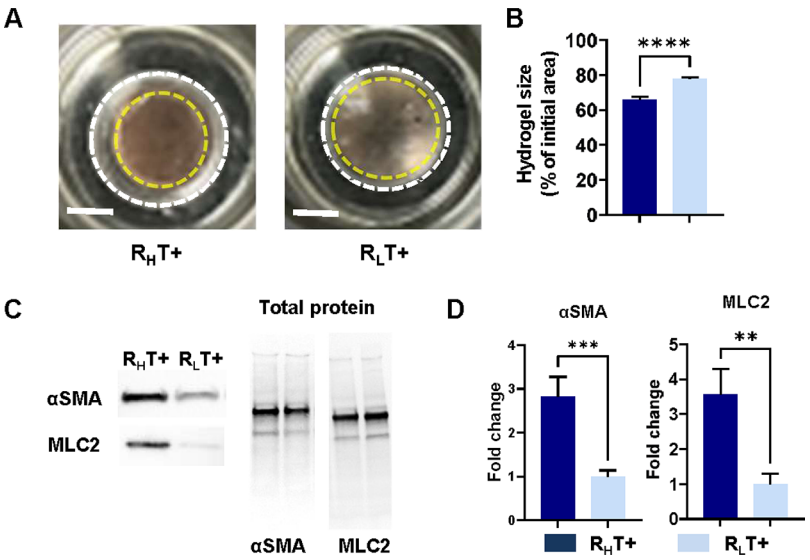

Figure 6. Characterization of day 14 constructs for cellular contractility (A, B) and the expression of αSMA and MLC2 (C, D). (A) Digital images of R_HT+ and R_LT+ constructs after 14 days of culture. White and yellow dotted circles outline the border of the day 0 and day 14 constructs, respectively. Scale bar: 2 mm. (B) Quantitative analysis of the degree of contraction. ****$p < 0.0001$ determined by Student's t test. (C) Detection of αSMA and MLC2 by Western blotting. (D) Quantitative analysis of Western blot bands by densitometry for αSMA and MLC2. **$p < 0.01$, ***$p < 0.001$, determined by Student's t test. All error bars represent standard error of the mean.

regulating the expression of integrin receptors and the focal adhesion molecule vinculin.[53,54] In our case, TGF-β1 stimulated a higher expression of integrin α_v (*ITGAV*, 1.34 ± 0.13 folds, $p < 0.05$) and vinculin (*VCL*, 1.22 ± 0.04 folds, $p < 0.01$) in R_HT+ cultures as compared to R_LT+ cultures on day 14, although the expression levels for integrins α_5 (*ITGA5*), β_1 (*ITGB1*), and β_3 (*ITGB3*) were comparable (Figure 5A). Additionally, cells maintained under R_HT+ conditions expressed a significantly ($p < 0.05$) higher level of genes encoding connective tissue growth factor (*CTGF*, 1.49 ± 0.15 folds, $p < 0.05$), hepatocyte growth factor (*HGF*, 1.88 ± 0.28 folds, $p < 0.01$), vascular endothelial growth factor A (*VEGFA*, 1.82 ± 0.27 folds, $p < 0.01$), and basic fibroblast growth factor (*bFGF*, 1.70 ± 0.30 folds, $p < 0.05$; Figure 5B), all of which are known to be involved in wound healing.[55,56] These results suggest that cells residing in R_H sECM are more receptive to TGF-β1 activation, with enhanced cell-matrix adhesion and elevated wound healing responses, possibly via cross-talk between the growth factors and integrin α_v receptors.[57−59]

The RGD density-dependent phenotypic change also prompted a significant ($p < 0.05$) upregulation of the expression of genes encoding ECM proteins (Figure 5C). Compared to the R_LT+ controls, R_HT+ cultures had 1.54 ± 0.20-, 1.51 ± 0.18-, 1.35 ± 0.14-, and 1.70 ± 0.30-fold increase in the expression of *COL1A1*, *COL1A2*, *COL3A1*, and *FN*, respectively, on day 14. Coincidently, the expression of these ECM proteins peaked during the initial proliferative phase of wound healing after an acute vocal fold injury.[5] On the other hand, the mRNA levels of proteins involved in ECM metabolism, *MMP1*, *MMP2*, and *TIMP1*, were not significantly altered between R_HT+ and R_LT+ cultures despite their disparate cell phenotypes (Figure 5C).

Examination of day 14 media for R_HT+ cultures by antibody arrays revealed the presence of TIMP2, VEGFA, IL-6, and IL-8 (Figure S37). The secretion of these proteins, along with procollagen 1α1, were further quantified using ELISA. Cellular production of these proteins was low under TGF-β1-free conditions, irrespective of the RGD density (R_HT- and R_LT-; Figure 5D−G). TGF-β1 significantly stimulated the production of pro-inflammatory cytokines (IL-6 and IL-8), a proangiogenic protein (VEGFA) and the precursor of a major ECM structural protein (procollagen 1α1). In all cases, the highest and most robust responses were detected in cultures with high RGD density (R_HT+). The positive correlation procollagen 1 and collagen type 1 has been documented *in vivo* in scarred tissues.[60−62] Again, TIMP2 secretion was consistent across the four types of cultures (Figure 5H).

Our results suggest that sECM with a high RGD concentration promoted cellular secretion of cytokines that in turn stimulated endogenous synthesis of native ECM proteins.[63,64] In other words, cell function is strongly dependent on the initial ground state they are exposed to. It is possible that the susceptibility of the covalently integrated SMR cross-linker to specific protease degradation overrode differentiation-induced changes in the secretion of MMPs and TIMPs.[65] Previous work has documented that CTGF-induced myofibroblast differentiation did not alter the secretion levels of MMP2 at both transcript and protein levels in protease-degradable hydrogel networks.[66] Considering that a proper balance between matrix synthesis and degradation is the key to scarless wound healing, while extensive deposition of ECM proteins is characteristic of tissue fibrosis,[60,67] our model is more representative of vocal fold scarring.

In addition to being a hallmark of the myofibroblast phenotype, the αSMA incorporations into F-actin stress fibers produce a strong contractile force, which is responsible for wound closure.[48] Because TGF-β1 and matrix adhesions are key regulators of cytoskeleton organization of actin,[52] we measured the surface areas of cellular constructs on day 0 and day 14. As shown in Figure 6A, the R_HT+ cultures exhibited a higher degree of gel contraction compared to the R_LT- cultures. Furthermore, myosin light chain 2 (MLC2) is known to modulate cell contractility by activating the cross-bridge cycling of actins.[42,68] Western blot results show that R_HT+ cultures exhibited a significantly ($p < 0.01$) increased

Accepted Manuscript
Version of record at: https://doi.org/10.1021/acsami.2c13852

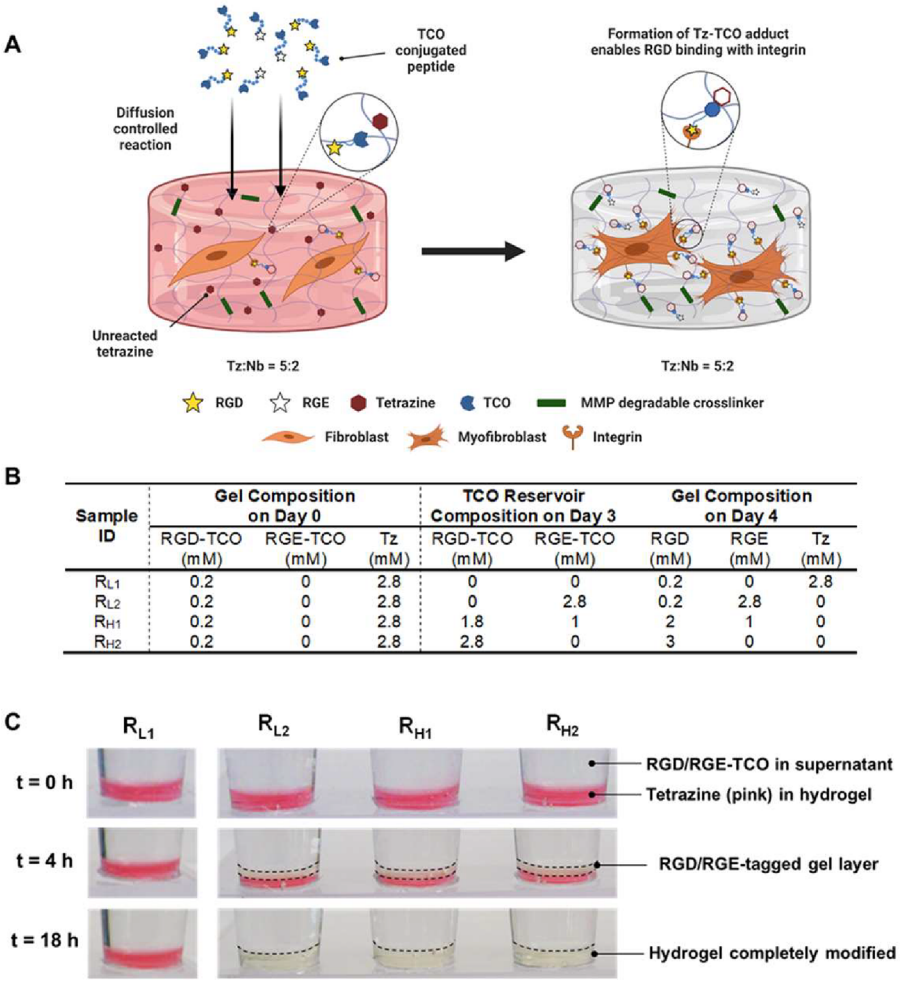

Sample ID	Gel Composition on Day 0			TCO Reservoir Composition on Day 3		Gel Composition on Day 4		
	RGD-TCO (mM)	RGE-TCO (mM)	Tz (mM)	RGD-TCO (mM)	RGE-TCO (mM)	RGD (mM)	RGE (mM)	Tz (mM)
R_{L1}	0.2	0	2.8	0	0	0.2	0	2.8
R_{L2}	0.2	0	2.8	0	2.8	0.2	2.8	0
R_{H1}	0.2	0	2.8	1.8	1	2	1	0
R_{H2}	0.2	0	2.8	2.8	0	3	0	0

Figure 7. Temporal modification of matrix adhesiveness under 3D cell culture conditions via diffusion-controlled bio-orthogonal ligation. (A) Schematic illustration of diffusion-controlled reaction in a cell-laden hydrogel. Created with BioRender.com. (B) Four different hydrogel constructs were produced from the original R_L constructs via tetrazine ligation at the gel−liquid interface using RGD/RGE-TCO. (C) Digital picture of the hydrogels showing the gradual disappearance of the pink color of tetrazine functional groups over time.

expression of both αSMA and MLC2, with 2.83 ± 0.45 and 3.57 ± 0.72 folds higher than R_LT+ controls (Figure 6C,D and Figures S39 and S40), respectively, indicative of the formation of contractile complexes.

Collectively, our results indicate that the highly adhesive sECM effectively primes the resident VFFs to undergo myofibroblast differentiation in response to TGF-β1 stimulation. It is generally recognized that the native ECM progressively becomes stiffened during the development of fibrotic diseases.[69,70] Fibroblasts cultured on stiff substrates with Young's moduli of greater than 20−50 kPa readily undergo myofibroblast differentiation.[71] Hydrogels investigated here are consistently soft and pliable, with an average G' of ∼120 P, yet robust myofibroblast differentiation is observed in R_HT+ cultures. Thus, matrix stiffening is not a determinant for fibroblast activation in our hydrogel platform. We speculate that a high density of the integrin binding motif in the cross-linked hydrogel network allows cells to be more strongly anchored via focal adhesion when activated by TGF-β1, thereby generating a higher level of tension.[51] Cell-generated tension further promotes integrin clustering and the formation of mature focal adhesion involving vinculin, paxillin, talin, and tensin.[51,72] This may induce the positive feedback loop in focal adhesion kinase (FAK) to alter the cytoskeleton architecture, reinforce tissue contractility, and increase cellular secretion of proteins and cytokines. In line with our findings, recent work by Matera et al.[15] shows that myofibroblast differentiation in 3D was inversely correlated with hydrogel stiffness but positively correlated with matrix fibers. In their composite hydrogel design, RGD was immobilized on the fibers, while the ground substance was MMP-degradable. Consequently, a higher fiber density means higher matrix adhesion.

3.4. Rapid Tetrazine Ligation Enables Delayed Activation of VFFs. After demonstrating the effect of sECM adhesiveness on myofibroblast differentiation, we queried whether myofibroblast differentiation could be induced in a temporal manner to mimic the dynamic phenotype switch during the early phase of wound healing. We have successfully applied tetrazine ligation to modify the stiffness and adhesiveness of sECM in real time during 3D culture.[18] Here, hydrogels with 0.2 mM RGD and 2.8 mM free tetrazines were prepared on day 0. Conditioned media with varying molar ratios of RGD-TCO/RGE-TCO was added to the top chamber of the cell culture insert to produce a modified construct with a final RGD concentration ranging from 0.2 to 3 mM (Figure 7A,B). For example, the premade hydrogel was bio-orthogonally modified with an additional 2.8 mM of RGE-TCO (0 mM RGD-TCO) to produce a construct

Accepted Manuscript
Version of record at: https://doi.org/10.1021/acsami.2c13852

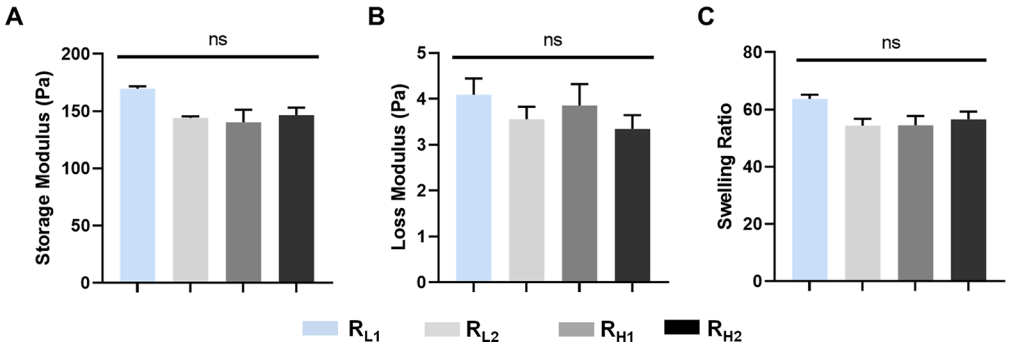

Figure 8. Characterization of mechanical properties of hydrogels prepared by diffusion-controlled reaction. (A, B) Storage (A) and loss (B) moduli for the modified hydrogels (three samples per group). (C) Swelling ratio as a function of hydrogel composition (three samples per group). ns indicates nonsignificant comparison determined by one-way ANOVA. All error bars represent the standard error of the mean.

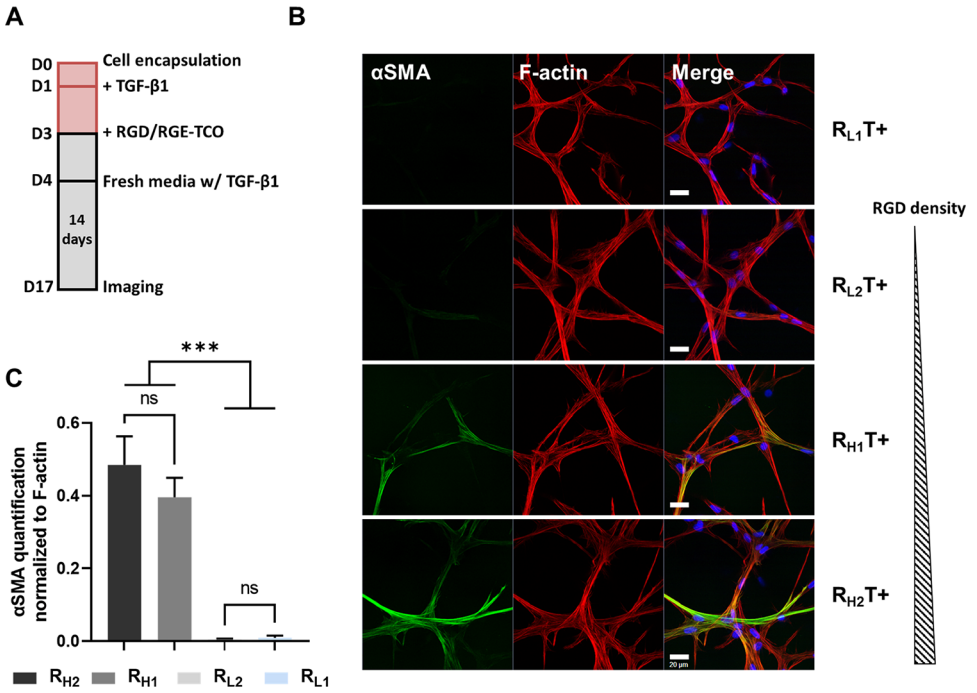

Figure 9. 3D cell culture of cell-laden hydrogel constructs with temporal increase of matrix adhesiveness. (A) Experimental timeline. On day 0, VFF-laden constructs with 0.2 mM RGD were prepared. On day 1, cultures were supplemented with 5 ng/mL TGF-β1. On day 3, RGD/RGE-TCO was added to the media to initiate diffusion-controlled reaction. On day 4, TCO media was replaced with TGF-β1-conditioned media. Media was refreshed every other day, and cultures were terminated on day 17. (B) Confocal images of day 17 cultures detailing the formation of αSMA stress fiber formation. αSMA, F-actin, and nuclei stained with green, red, and blue, respectively. Scale bar: 20 μm. (C) Quantification of αSMA expression as the integrated density ratio between αSMA and F-actin signals. The sum of the fluorescent intensities for αSMA was normalized to that for F-actin. ***$p < 0.001$, ns: nonsignificant, determined by one-way ANOVA. $n = 5$. All error bars represent the standard error of the mean.

with 0.2 mM immobilized RGD (R_{L2}). When a solution containing 1.8 mM RGD-TCO and 1.0 mM RGE-TCO was used, the initial gel with low RGD content was transformed to R_{H1} with a final RGD concentration of 2.0 mM. Similarly, treatment of the bulk gel with 2.8 mM of RGD-TCO (0 mM RGE-TCO) resulted in the establishment of constructs with a final RGD concentration of 3 mM (R_{H2}). Incubation of the initial bulk gel in media without any TCO species produced the R_{L1} controls. Under these conditions, diffusion occurred in one dimension driven by the concentration gradient.

Successful conjugation of additional RGD and RGE motifs was confirmed by the gradual disappearance of the pink tetrazine chromophore (Figure 7C). After overnight incubation, the pink color disappeared completely, indicating a complete transformation of the remaining tetrazine groups (pink) to stable cycloadducts (slightly yellow). Because tetrazine−TCO reaction at the gel/liquid interface is instantaneous, while the diffusion of TCO species through the cross-linked network is slow, the conjugation reaction is diffusion-controlled. Because RGD-TCO and RGE-TCO exhibited a comparable molecular weight, the time required for the establishment of all four hydrogels is the same. Theoretically, one can introduce additional bioactive signals to the cell-laden hydrogel construct at any time during cell culture because of the stability of the tetrazine group and the biorthogonality of the tetrazine-TCO reaction.[18,29]

Upon completion of tetrazine ligation, hydrogels were analyzed by oscillatory shear rheometry (Figure 8A,B). Converting the remaining 2.8 mM free tetrazines in R_{L1} to dangling RGE motifs in R_{L2} did not significantly alter the

Accepted Manuscript
Version of record at: https://doi.org/10.1021/acsami.2c13852

hydrogel mechanical properties. Furthermore, gels prepared with different ratios of RGD-TCO and RGE-TCO (R_{L1}, R_{H1}, and R_{H2}) exhibited comparable viscoelastic properties (Figure S41). The equilibrium swelling ratios for all four types of hydrogels were similar (Figure 8C). The dangling RGD/RGE peptides are non-elastically active and do not contribute to the network integrity. Overall, the diffusion-controlled biorthogonal ligation method enabled temporal modulation of matrix adhesiveness without altering their mechanical properties.

To evaluate myofibroblast differentiation in the dynamic environment, cell-laden hydrogel constructs were cultured under conditions outlined in Figure 9A. First, VFFs were encapsulated in hydrogels with 0.2 mM RGD on day 0, and from day 1 to day 17, constructs were maintained in TGF-β1-supplemented media. To recapitulate the enhanced fibronectin deposition during the overlapping inflammatory and proliferative phases of vocal fold wound healing,[5] media containing varying amounts of RGD-TCO and RGE-TCO was added on top of the construct to initiate the reaction at the gel−liquid interface on day 3. A day later, the TCO-containing media was replaced with fresh cell culture media, and VFFs were cultured for another 14 days in the presence of TGF-β1. As the RGD density increased in a timely manner, the formation of αSMA stress fiber was observed on day 17 (Figure 9B). This is consistent with our earlier finding with R_HT+ samples, where all RGD signals were introduced at day 0. A comparison between $R_{L1}T$+ and $R_{L2}T$+ cultures showed that the diffusion-controlled reaction did not affect αSMA expression; minimal myofibroblast differentiation was observed at a low RGD concentration. Time-delayed alteration of RGD concentration from 0.2 mM to 2 or 3 mM led to the most robust expression of αSMA. Cellular expression of αSMA in R_{H1} (0.396 ± 0.054) and R_{H2} (0.484 ± 0.079) cultures was significantly higher ($p < 0.001$) than those in R_{L1} (0.009 ± 0.006) and R_{L2} (0.005 ± 0.002) (Figure 9C). Although the αSMA expression was slightly higher in R_{H2} (with 3 mM RGD) than in R_{H1} (with 2 mM RGD) constructs, the difference was not statistically significant. Follow-up mechanistic investigations have to be performed to understand as to what extent the time-delayed introduction of cell adhesion sites affect myofibroblast differentiation and how. Overall, a time-delayed modification using tetrazine−TCO ligation allowed for the temporal introduction of fibronectin-derived peptides to the cell-laden hydrogel constructs. Given our observation that the alteration of matrix adhesiveness induced myofibroblast differentiation as occurring during wound healing progress, we show that our engineered in vitro tissue model can serve as a valuable tool for studying molecular mechanisms associated with vocal fold wound healing and for developing targeted therapeutic intervention strategies for vocal fold scarring.

4. CONCLUSIONS

Using dienophiles with different reactivities toward tetrazine, we demonstrated a novel strategy to alter the matrix adhesiveness in a 3D engineered hydrogel platform. While the slower tetrazine−norbornene ligation permitted 3D cell encapsulation, the faster tetrazine−TCO ligation facilitated the efficient conjugation of integrin-binding peptides to the hydrogel networks. In addition, the stability of the tetrazine functional group combined with the superior reactivity of TCO derivatives enabled temporal increase of cell binding motifs in cell-laden hydrogel constructs, recapitulating the dynamic alteration of ECM properties during the early stage of wound healing. The matrices with a high RGD density prompted the highest level of myofibroblast differentiation with the formation of αSMA-integrated actin cytoskeleton network, development of cell contractility, and secretion of pro-inflammatory cytokines, pro-angiogenic factors, and ECM proteins. These findings confirm a clear influence of matrix adhesiveness on myofibroblast differentiation and furthermore imply that our bio-orthogonal in vitro hydrogel platform can mimic pathogenic factors observed during the progression of wound healing.

ASSOCIATED CONTENT

Supporting Information

The Supporting Information is available free of charge at https://pubs.acs.org/doi/10.1021/acsami.2c13852.

Methods, schemes and chromatography/spectroscopy characterization of compounds and macromolecules used in this study; list of qPCR primers; standard curves used for the characterization of peptide conjugation efficiency; representative rheological data; cytokine array results; quantification of protein content by BCA assay; original Western blot results (PDF)

AUTHOR INFORMATION

Corresponding Author

Xinqiao Jia − *Department of Materials Science and Engineering and Department of Biomedical Engineering, University of Delaware, Newark, Delaware 19716, United States; Delaware Biotechnology Institute, Newark, Delaware 19716, United States;* orcid.org/0000-0002-3564-5576; Phone: 302-831-6553; Email: xjia@udel.edu; Fax: 302-831-4545

Authors

Jiyeon Song − *Department of Materials Science and Engineering, University of Delaware, Newark, Delaware 19716, United States;* orcid.org/0000-0003-1822-8006

Hanyuan Gao − *Department of Materials Science and Engineering, University of Delaware, Newark, Delaware 19716, United States*

He Zhang − *Department of Materials Science and Engineering, University of Delaware, Newark, Delaware 19716, United States;* orcid.org/0000-0003-1165-6702

Olivia J. George − *Department of Materials Science and Engineering, University of Delaware, Newark, Delaware 19716, United States*

Ashlyn S. Hillman − *Department of Chemistry and Biochemistry, University of Delaware, Newark, Delaware 19716, United States*

Joseph M. Fox − *Department of Materials Science and Engineering and Department of Chemistry and Biochemistry, University of Delaware, Newark, Delaware 19716, United States;* orcid.org/0000-0002-8258-1640

Complete contact information is available at: https://pubs.acs.org/10.1021/acsami.2c13852

Notes

The authors declare no competing financial interest.

ACKNOWLEDGMENTS

This work was supported in part by the National Institutes of Health (NIDCD R01DC014461 and NIDCR R01DE029655),

National Science Foundation (NSF, DMR 1809612), and the Delaware Bioscience Center for Advanced Technology (DE-CAT 12A00448). Instrumentation and core facility support was made possible by NIH (S10 OD016361, P20 GM103446, and P20GM139760) and NSF (CHE-0840401, CHE-1229234, and IIA-1301765) grants. The authors also acknowledge the use of facilities and instrumentation supported by NSF through the University of Delaware Materials Research Science and Engineering Center (DMR-2011824).

REFERENCES

(1) Hirano, M. Morphological structure of the vocal cord as a vibrator and its variations. *Folia phoniatrica et logopaedica* **1974**, *26*, 89−94.
(2) Friedrich, G.; Dikkers, F.; Arens, C.; Remacle, M.; Hess, M.; Giovanni, A.; Duflo, S.; Hantzakos, A.; Bachy, V.; Gugatschka, M. Vocal fold scars: current concepts and future directions. Consensus report of the Phonosurgery Committee of the European Laryngological Society. *Eur. Arch. Otorhinolaryngol.* **2013**, *270*, 2491−2507.
(3) Gray, S. D. Cellular physiology of the vocal folds. *Otolaryngol. Clin. North Am.* **2000**, *33*, 679−697.
(4) Catten, M.; Gray, S. D.; Hammond, T. H.; Zhou, R.; Hammond, E. Analysis of cellular location and concentration in vocal fold lamina propria. *Otolaryngol Head Neck Surg.* **1998**, *118*, 663−667.
(5) Tateya, T.; Tateya, I.; Sohn, J. H.; Bless, D. M. Histological study of acute vocal fold injury in a rat model. *Ann. Otol., Rhinol., Laryngol.* **2006**, *115*, 285−292.
(6) Hu, R.; Xu, W.; Ling, W.; Wang, Q.; Wu, Y.; Han, D. Characterization of extracellular matrix proteins during wound healing in the lamina propria of vocal fold in a canine model: a long-term and consecutive study. *Acta Histochem.* **2014**, *116*, 730−735.
(7) Hirschi, S. D.; Gray, S. D.; Thibeault, S. L. Fibronectin: an interesting vocal fold protein. *J. Voice* **2002**, *16*, 310−316.
(8) Hirano, S.; Bless, D. M.; Rousseau, B.; Welham, N.; Scheidt, T.; Ford, C. N. Fibronectin and adhesion molecules on canine scarred vocal folds. *Laryngoscope* **2003**, *113*, 966−972.
(9) Przekora, A. A concise review on tissue engineered artificial skin grafts for chronic wound treatment: can we reconstruct functional skin tissue in vitro? *Cell* **2020**, *9*, 1622.
(10) Johns, M. M.; Kolachala, V.; Berg, E.; Muller, S.; Creighton, F. X.; Branski, R. C. Radiation fibrosis of the vocal fold: from man to mouse. *Laryngoscope* **2012**, *122*, SS107−SS125.
(11) Cao, H.; Duan, L.; Zhang, Y.; Cao, J.; Zhang, K. Current hydrogel advances in physicochemical and biological response-driven biomedical application diversity. *Signal Transduction Targeted Ther.* **2021**, *6*, 1−31.
(12) Matera, D. L.; Wang, W. Y.; Baker, B. M. New directions and dimensions for bioengineered models of fibrosis. *Nat. Rev. Mater.* **2021**, *6*, 192−195.
(13) Kosinski, A. M.; Sivasankar, M. P.; Panitch, A. Varying RGD concentration and cell phenotype alters the expression of extracellular matrix genes in vocal fold fibroblasts. *J. Biomed. Mater. Res., Part A* **2015**, *103*, 3094−3100.
(14) Davidson, M. D.; Song, K. H.; Lee, M.-H.; Llewellyn, J.; Du, Y.; Baker, B. M.; Wells, R. G.; Burdick, J. A. Engineered fibrous networks to investigate the influence of fiber mechanics on myofibroblast differentiation. *ACS Biomater. Sci. Eng.* **2019**, *5*, 3899−3908.
(15) Matera, D. L.; DiLillo, K. M.; Smith, M. R.; Davidson, C. D.; Parikh, R.; Said, M.; Wilke, C. A.; Lombaert, I. M.; Arnold, K. B.; Moore, B. B.; Baker, B. M. Microengineered 3D pulmonary interstitial mimetics highlight a critical role for matrix degradation in myofibroblast differentiation. *Sci. Adv.* **2020**, *6*, No. eabb5069.
(16) Seo, B. R.; Chen, X.; Ling, L.; Song, Y. H.; Shimpi, A. A.; Choi, S.; Gonzalez, J.; Sapudom, J.; Wang, K.; Andresen Eguiluz, R. C.; Gourdon, D.; Shenoy, V. B.; Fischbach, C. Collagen microarchitecture mechanically controls myofibroblast differentiation. *Proc. Natl. Acad. Sci.* **2020**, *117*, 11387−11398.
(17) Ma, H.; Caldwell, A. S.; Azagarsamy, M. A.; Gonzalez Rodriguez, A.; Anseth, K. S. Bioorthogonal click chemistries enable simultaneous spatial patterning of multiple proteins to probe synergistic protein effects on fibroblast function. *Biomaterials* **2020**, *255*, No. 120205.
(18) Hao, Y.; Song, J.; Ravikrishnan, A.; Dicker, K. T.; Fowler, E. W.; Zerdoum, A. B.; Li, Y.; Zhang, H.; Rajasekaran, A. K.; Fox, J. M.; Jia, X. Rapid bioorthogonal chemistry enables in situ modulation of the stem cell behavior in 3d without external triggers. *ACS Appl. Mater. Interfaces* **2018**, *10*, 26016−26027.
(19) Selvaraj, R.; Fox, J. M. trans-Cyclooctene—a stable, voracious dienophile for bioorthogonal labeling. *Curr. Opin. Chem. Biol.* **2013**, *17*, 753−760.
(20) Devaraj, N. K.; Weissleder, R.; Hilderbrand, S. A. Tetrazine-based cycloadditions: application to pretargeted live cell imaging. *Bioconjugate Chem.* **2008**, *19*, 2297−2299.
(21) Lang, K.; Davis, L.; Wallace, S.; Mahesh, M.; Cox, D. J.; Blackman, M. L.; Fox, J. M.; Chin, J. W. Genetic encoding of bicyclononynes and trans-cyclooctenes for site-specific protein labeling in vitro and in live mammalian cells via rapid fluorogenic Diels−Alder reactions. *J. Am. Chem. Soc.* **2012**, *134*, 10317−10320.
(22) Wang, M.; Svatunek, D.; Rohlfing, K.; Liu, Y.; Wang, H.; Giglio, B.; Yuan, H.; Wu, Z.; Li, Z.; Fox, J. Conformationally strained trans-cyclooctene (sTCO) enables the rapid construction of 18F-PET probes via tetrazine ligation. *Theranostics* **2016**, *6*, 887.
(23) Liu, S.; Moore, A. C.; Zerdoum, A. B.; Zhang, H.; Scinto, S. L.; Zhang, H.; Gong, L.; Burris, D. L.; Rajasekaran, A. K.; Fox, J. M.; Jia, X. Cellular interactions with hydrogel microfibers synthesized via interfacial tetrazine ligation. *Biomaterials* **2018**, *180*, 24−35.
(24) Ravikrishnan, A.; Zhang, H.; Fox, J. M.; Jia, X. Core−shell Microfibers via bioorthogonal layer-by-layer assembly. *ACS Macro Lett.* **2020**, *9*, 1369−1375.
(25) Wang, D.; Chen, W.; Zheng, Y.; Dai, C.; Wang, K.; Ke, B.; Wang, B. 3, 6-Substituted-1, 2, 4, 5-tetrazines: tuning reaction rates for staged labeling applications. *Org. Biomol. Chem.* **2014**, *12*, 3950−3955.
(26) Darko, A.; Wallace, S.; Dmitrenko, O.; Machovina, M. M.; Mehl, R. A.; Chin, J. W.; Fox, J. M. Conformationally strained trans-cyclooctene with improved stability and excellent reactivity in tetrazine ligation. *Chem. Sci.* **2014**, *5*, 3770−3776.
(27) Royzen, M.; Yap, G. P. A.; Fox, J. M. A photochemical synthesis of functionalized trans-cyclooctenes driven by metal complexation. *J. Am. Chem. Soc.* **2008**, *130*, 3760−3761.
(28) Taylor, M. T.; Blackman, M. L.; Dmitrenko, O.; Fox, J. M. Design and synthesis of highly reactive dienophiles for the tetrazine−trans-cyclooctene ligation. *J. Am. Chem. Soc.* **2011**, *133*, 9646−9649.
(29) Dicker, K.; Song, J.; Moore, A.; Zhang, H.; Li, Y.; Burris, D.; Jia, X.; Fox, J. Core−shell patterning of synthetic hydrogels via interfacial bioorthogonal chemistry for spatial control of stem cell behavior. *Chem. Sci.* **2018**, *9*, 5394−5404.
(30) Ruoslahti, E. Fibronectin and its receptors. *Annu. Rev. Biochem.* **1988**, *57*, 375−413.
(31) Fowler, E. W.; Ravikrishnan, A.; Witt, R. L.; Pradhan-Bhatt, S.; Jia, X. RGDSP-Decorated Hyaluronate Hydrogels Facilitate Rapid 3D Expansion of Amylase-Expressing Salivary Gland Progenitor Cells. *ACS Biomater. Sci. Eng.* **2021**, *7*, 5749−5761.
(32) Ravikrishnan, A.; Fowler, E. W.; Stuffer, A. J.; Jia, X. Hydrogel-supported, engineered model of vocal fold epithelium. *ACS Biomater. Sci. Eng.* **2021**, *7*, 4305−4317.
(33) Hwang, J.; Kiick, K. L.; Sullivan, M. O. Modified hyaluronic acid-collagen matrices trigger efficient gene transfer and prohealing behavior in fibroblasts for improved wound repair. *Acta Biomater.* **2022**, 138.
(34) Wang, S.; Wang, B.; He, H.; Sun, A.; Guo, C. A new set of reference housekeeping genes for the normalization RT-qPCR data from the intestine of piglets during weaning. *PLoS One* **2018**, *13*, No. e0204583.
(35) Aldridge, G. M.; Podrebarac, D. M.; Greenough, W. T.; Weiler, I. J. The use of total protein stains as loading controls: an alternative

to high-abundance single-protein controls in semi-quantitative immunoblotting. *J. Neurosci. Methods* **2008**, *172*, 250−254.
(36) Nie, X.; Li, C.; Hu, S.; Xue, F.; Kang, Y. J.; Zhang, W. An appropriate loading control for western blot analysis in animal models of myocardial ischemic infarction. *Biochem. Biophys. Rep.* **2017**, *12*, 108−113.
(37) Gray, S. D.; Titze, I. R.; Chan, R.; Hammond, T. H. Vocal fold proteoglycans and their influence on biomechanics. *Laryngoscope* **1999**, *109*, 845−854.
(38) Chan, R. W.; Titze, I. R. Viscoelastic shear properties of human vocal fold mucosa: theoretical characterization based on constitutive modeling. *J. Acoust. Soc. Am.* **2000**, *107*, 565−580.
(39) Darling, N. J.; Hung, Y.-S.; Sharma, S.; Segura, T. Controlling the kinetics of thiol-maleimide Michael-type addition gelation kinetics for the generation of homogenous poly (ethylene glycol) hydrogels. *Biomaterials* **2016**, *101*, 199−206.
(40) Yun, Y.-R.; Won, J. E.; Jeon, E.; Lee, S.; Kang, W.; Jo, H.; Jang, J.-H.; Shin, U. S.; Kim, H.-W. Fibroblast growth factors: biology, function, and application for tissue regeneration. *J. Tissue Eng.* **2010**, *1*, No. 218142.
(41) Dolivo, D. M.; Larson, S. A.; Dominko, T. Fibroblast growth factor 2 as an antifibrotic: antagonism of myofibroblast differentiation and suppression of pro-fibrotic gene expression. *Cytokine Growth Factor Rev.* **2017**, *38*, 49−58.
(42) Pakshir, P.; Noskovicova, N.; Lodyga, M.; Son, D. O.; Schuster, R.; Goodwin, A.; Karvonen, H.; Hinz, B. The myofibroblast at a glance. *J. Cell Sci.* **2020**, *133*, jcs227900.
(43) Dicker, K. T.; Moore, A. C.; Garabedian, N. T.; Zhang, H.; Scinto, S. L.; Akins, R. E.; Burris, D. L.; Fox, J. M.; Jia, X. Spatial patterning of molecular cues and vascular cells in fully integrated hydrogel channels via interfacial bioorthogonal cross-linking. *ACS Appl. Mater. Interfaces* **2019**, *11*, 16402−16411.
(44) Melchionna, R.; Trono, P.; Tocci, A.; Nisticò, P. Actin cytoskeleton and regulation of TGFβ signaling: exploring their links. *Biomolecules* **2021**, *11*, 336.
(45) Chen, X.; Thibeault, S. L. Response of fibroblasts to transforming growth factor-β1 on two-dimensional and in three-dimensional hyaluronan hydrogels. *Tissue Eng., Part A* **2012**, *18*, 2528−2538.
(46) Branton, M. H.; Kopp, J. B. TGF-β and fibrosis. *Microbes Infect.* **1999**, *1*, 1349−1365.
(47) Border, W. A.; Noble, N. A. Transforming growth factor β in tissue fibrosis. *N. Engl. J. Med.* **1994**, *331*, 1286−1292.
(48) Hinz, B.; Celetta, G.; Tomasek, J. J.; Gabbiani, G.; Chaponnier, C. Alpha-smooth muscle actin expression upregulates fibroblast contractile activity. *Mol. Biol. Cell* **2001**, *12*, 2730−2741.
(49) Gabasa, M.; Duch, P.; Jorba, I.; Giménez, A.; Lugo, R.; Pavelescu, I.; Rodríguez-Pascual, F.; Molina-Molina, M.; Xaubet, A.; Pereda, J.; Alcaraz, J. Epithelial contribution to the profibrotic stiff microenvironment and myofibroblast population in lung fibrosis. *Mol. Biol. Cell* **2017**, *28*, 3741−3755.
(50) Tay, C. Y.; Wu, Y.-L.; Cai, P.; Tan, N. S.; Venkatraman, S. S.; Chen, X.; Tan, L. P. Bio-inspired micropatterned hydrogel to direct and deconstruct hierarchical processing of geometry-force signals by human mesenchymal stem cells during smooth muscle cell differentiation. *NPG Asia Mater.* **2015**, *7*, e199−e199.
(51) Goffin, J. M.; Pittet, P.; Csucs, G.; Lussi, J. W.; Meister, J.-J.; Hinz, B. Focal adhesion size controls tension-dependent recruitment of α-smooth muscle actin to stress fibers. *J. Cell Biol.* **2006**, *172*, 259−268.
(52) Sandbo, N.; Dulin, N. Actin cytoskeleton in myofibroblast differentiation: ultrastructure defining form and driving function. *Transl. Res.* **2011**, *158*, 181−196.
(53) Zent, J.; Guo, L.-W. Signaling mechanisms of myofibroblastic activation: outside-in and inside-out. *Cell. Physiol. Biochem.* **2018**, *49*, 848−868.
(54) Rout, U. K.; Saed, G. M.; Diamond, M. P. Transforming growth factor-β1 modulates expression of adhesion and cytoskeletal proteins in human peritoneal fibroblasts. *Fertil. Steril.* **2002**, *78*, 154−161.
(55) Barrientos, S.; Stojadinovic, O.; Golinko, M. S.; Brem, H.; Tomic-Canic, M. Growth factors and cytokines in wound healing. *Wound Repair Regen.* **2008**, *16*, 585−601.
(56) Hirano, S.; Thibeault, S.; Ford, C. N.; Bless, D. M.; Kanemaru, S.-I. Hepatocyte growth factor and its receptor c-met in rat and rabbit vocal folds. *Ann. Otol., Rhinol., Laryngol.* **2002**, *111*, 661−666.
(57) Eliceiri, B. P. Integrin and growth factor receptor crosstalk. *Circ. Res.* **2001**, *89*, 1104−1110.
(58) Chan, P.-C.; Chen, S.-Y.; Chen, C.-H.; Chen, H.-C. Crosstalk between hepatocyte growth factor and integrin signaling pathways. *J. Biomed. Sci.* **2006**, *13*, 215−223.
(59) Hendesi, H.; Barbe, M. F.; Safadi, F. F.; Monroy, M. A.; Popoff, S. N. Integrin mediated adhesion of osteoblasts to connective tissue growth factor (CTGF/CCN2) induces cytoskeleton reorganization and cell differentiation. *PLoS One* **2015**, *10*, No. e0115325.
(60) Yamashita, M.; Bless, D. M.; Welham, N. V. Morphological and extracellular matrix changes following vocal fold injury in mice. *Cells Tissues Organs* **2010**, *192*, 262−271.
(61) Rousseau, B.; Hirano, S.; Scheidt, T. D.; Welham, N. V.; Thibeault, S. L.; Chan, R. W.; Bless, D. M. Characterization of vocal fold scarring in a canine model. *Laryngoscope* **2003**, *113*, 620−627.
(62) Riaz, Y.; Cook, H.; Wangoo, A.; Glenville, B.; Shaw, R. Type 1 procollagen as a marker of severity of scarring after sternotomy: effects of topical corticosteroids. *J. Clin. Pathol.* **1994**, *47*, 892−899.
(63) Johnson, B. Z.; Stevenson, A. W.; Prêle, C. M.; Fear, M. W.; Wood, F. M. The role of IL-6 in skin fibrosis and cutaneous wound healing. *Biomedicines* **2020**, *8*, 101.
(64) Zgheib, C.; Xu, J.; Liechty, K. W. Targeting inflammatory cytokines and extracellular matrix composition to promote wound regeneration. *Adv. Wound Care* **2014**, *3*, 344−355.
(65) Patterson, J.; Hubbell, J. A. Enhanced proteolytic degradation of molecularly engineered PEG hydrogels in response to MMP-1 and MMP-2. *Biomaterials* **2010**, *31*, 7836−7845.
(66) Zerdoum, A. B.; Fowler, E. W.; Jia, X. Induction of fibrogenic phenotype in human mesenchymal stem cells by connective tissue growth factor in a hydrogel model of soft connective tissue. *ACS Biomater. Sci. Eng.* **2019**, *5*, 4531−4541.
(67) Kishimoto, Y.; Kishimoto, A. O.; Ye, S.; Kendziorski, C.; Welham, N. V. Modeling fibrosis using fibroblasts isolated from scarred rat vocal folds. *Lab. Invest.* **2016**, *96*, 807−816.
(68) Sheikh, F.; Lyon, R. C.; Chen, J. Functions of myosin light chain-2 (MYL2) in cardiac muscle and disease. *Gene* **2015**, *569*, 14−20.
(69) Huang, X.; Yang, N.; Fiore, V. F.; Barker, T. H.; Sun, Y.; Morris, S. W.; Ding, Q.; Thannickal, V. J.; Zhou, Y. Matrix stiffness−induced myofibroblast differentiation is mediated by intrinsic mechanotransduction. *Am. J. Respir. Cell Mol. Biol.* **2012**, *47*, 340−348.
(70) Cox, T. R.; Erler, J. T. Remodeling and homeostasis of the extracellular matrix: implications for fibrotic diseases and cancer. *Dis. Models Mech.* **2011**, *4*, 165−178.
(71) D'Urso, M.; Kurniawan, N. A. Mechanical and physical regulation of fibroblast−myofibroblast transition: From cellular mechanoresponse to tissue pathology. *Front. Bioeng. Biotechnol.* **2020**, *8*, 609653.
(72) Dugina, V.; Fontao, L.; Chaponnier, C.; Vasiliev, J.; Gabbiani, G. Focal adhesion features during myofibroblastic differentiation are controlled by intracellular and extracellular factors. *J. Cell Sci.* **2001**, *114*, 3285−3296.